Annales Geophysicae (2004) 22: 2115–2133
SRef-ID: 1432-0576/ag/2004-22-2115

Annales Geophysicae

Ion shell distributions as free energy source for plasma waves on auroral field lines mapping to plasma sheet boundary layer

A. Olsson[1], **P. Janhunen**[2], **and W. K. Peterson**[3]

[1]Swedish Institute of Space Physics, Uppsala Division, Uppsala, Sweden
[2]Finnish Meteorological Institute, Geophysical Research, Helsinki, Finland
[3]LASP, University of Colorado, Boulder, Colorado, USA

Received: 1 September 2003 – Revised: 4 December 2003 – Accepted: 23 January 2004 – Published: 14 June 2004

Abstract. Ion shell distributions are hollow spherical shells in velocity space that can be formed by many processes and occur in several regions of geospace. They are interesting because they have free energy that can, in principle, be transmitted to ions and electrons. Recently, a technique has been developed to estimate the original free energy available in shell distributions from in-situ data, where some of the energy has already been lost (or consumed). We report a systematic survey of three years of data from the Polar satellite. We present an estimate of the free energy available from ion shell distributions on auroral field lines sampled by the Polar satellite below 6 R_E geocentric radius. At these altitudes the type of ion shells that we are especially interested in is most common on auroral field lines close to the polar cap (i.e. field lines mapping to the plasma sheet boundary layer, PSBL). Our analysis shows that ion shell distributions that have lost some of their free energy are commonly found not only in the PSBL, but also on auroral field lines mapping to the boundary plasma sheet (BPS), especially in the evening sector auroral field lines. We suggest that the PSBL ion shell distributions are formed during the so-called Velocity Dispersed Ion Signatures (VDIS) events. Furthermore, we find that the partly consumed shells often occur in association with enhanced wave activity and middle-energy electron anisotropies. The maximum downward ion energy flux associated with a shell distribution is often 10 mW m^{-2} and sometimes exceeds 40 mW m^{-2} when mapped to the ionosphere and thus may be enough to power many auroral processes. Earlier simulation studies have shown that ion shell distributions can excite ion Bernstein waves which, in turn, energise electrons in the parallel direction. It is possible that ion shell distributions are the link between the X-line and the auroral wave activity and electron acceleration in the energy transfer chain for stable auroral arcs.

Key words. Magnetospheric physics (plasma sheet; auroral phenomena) – Space plasma physics (wave-particle interactions)

Correspondence to: A. Olsson
(ao@irfu.se)

1 Introduction

Ion shell distributions are spherical shells in velocity space. They can be formed by many processes of which the most widely studied is the pickup process which occurs when the solar wind protons undergo a charge-exchange reaction with almost stationary neutrals. The slow ion resulting from the charge exchange is accelerated (picked up) by the solar wind electric field. Each ion will have the same magnitude of the velocity and after some pitch angle scattering process the other velocity components are randomised, resulting in a shell distribution. This mechanism has been studied in different contexts, including comets (Karimabadi et al., 1994) and the termination shock of the heliosphere (Kucharek and Scholer, 1995).

Inside the magnetosphere, shell distributions have not yet been studied much. Bingham et al. (1999), referring to Freja data published by Eliasson et al. (1994), discussed hot ion shell distributions with a loss cone at low altitude (which they called horseshoe distributions) and found that such distributions can generate lower hybrid waves. Ion shell distributions with dual loss cones have been discussed by Engebretson et al. (2002). They noted that these double loss cone distributions (which have been called toroidal by some investigators) at sub-auroral latitudes are maintained by transport from the plasma sheet and are possibly the free energy source of various pulsation modes. Janhunen et al. (2003a) provided examples of shell distributions in auroral latitudes at ∼4–5 R_E radial distance (geocentric distance) using Polar/TIMAS data and showed with the help of solving the linear dispersion relation numerically and by using a two-dimensional particle simulation that the observed shell distribution is unstable to a broad range of ion Bernstein wave modes. It was also shown in the paper that the generated Bernstein waves accelerate ∼100 eV electrons at a rate of ∼80 eV/s.

Velocity-dispersed ion signatures (VDIS) have been studied in the plasma-sheet boundary layer (PSBL) by many authors (Elphic and Gary, 1990; Baumjohann et al., 1990; Zelenyi et al., 1990; Bosqued et al., 1993a, b; Onsager and Mukai, 1995). By VDIS one refers to events in the PSBL where the ion energy increases towards the polar cap

boundary when measured by a satellite traversing through the auroral zone towards increasing latitude. The origin of the VDIS ions is assumed to be the small B_z region in the magnetotail, i.e. the region where the ions do not follow adiabatic trajectories (Bosqued et al., 1993a, b; Ashour-Abdalla et al., 1992). VDIS energy-latitude slopes have been used to find the location of the X-line, for example, Zelenyi et al. (1990). Test particle calculations and observations show that deep in the magnetotail, the VDIS ions are decomposed of beamlets that can be labelled by two integers: the order of the κ parameter resonance and the number of bounces the beamlet has made (Ashour-Abdalla et al., 1995). Each beamlet has a different energy (field-aligned velocity) and, therefore, the perpendicular convection mixes and reorders the beamlets, causing a mosaic structure (Ashour-Abdalla et al., 1995). At lower altitude, the three-dimensional ion distribution function corresponding to VDIS has not been directly addressed in the literature. Our analysis suggests that the ion shell distributions seen in the Polar/TIMAS 6 R_E radial distance in the PSBL form a VDIS when considered in the energy-latitude plane.

We use the following naming of zones when moving from high to low invariant latitudes. The plasma sheet boundary layer (PSBL) is the narrow ($\sim$1°) plasma sheet layer next to the polar cap containing VDIS as explained above. The boundary plasma sheet (BPS) is a wider region (several degrees) mapping to discrete auroral arcs (Winningham et al., 1975). On its low-latitude side is the central plasma sheet (CPS), mapping to diffuse aurora. The CPS is adjacent to the radiation belt (not discussed in this paper). The CPS/BPS boundary is usually difficult to determine unambiguously from satellite data above the acceleration region. Our terminology is similar to that used by Winningham et al. (1975), except that Winningham does not have a PSBL between his BPS and polar cap. Our terminology differs from, for example, Zelenyi et al. (1990) in that their PSBL is wider than our PSBL, containing also parts of our BPS.

The main emphasis of the paper is in the PSBL and BPS ion shells. In addition, it is found that shell distributions also occur in the CPS. In order to meaningfully discuss the properties of PSBL and BPS shells, it is necessary to also present some of the properties of the CPS shells. Physical causes and effects of CPS shells are outside the scope of the paper, however. Separate papers should be reserved for these important topics.

Our motivation for studying shell distributions in the auroral zone is that such distributions potentially contain a lot of free energy. Janhunen et al. (2003a) have shown that wave modes exist in the region which can tap this free energy. They have also developed a technique to estimate the available free energy from in-situ data. If significant tapping of the shell distribution free energy takes place, the total power transferred through shell distributions to waves and later to the electrons may be sufficient for powering some visible auroral features. The occurrence frequency of ion shells in the auroral zone is studied in the paper and the results show that the frequency (free energy density $>20\,\mathrm{eV\,cm^{-3}}$) in the PSBL is about 5%, spread over a few degrees ILAT, since the polar cap boundary location varies from case to case. The frequency of ion shells on auroral field lines mapping to the BPS is, however, small (since most shells are "partially consumed" here). When a method for estimating the original free energy from partial ion shells is applied, the occurrence frequency in this region increases.

The structure of the paper is as follows. After describing the relevant Polar satellite instruments and data processing we approach the ion shell distributions from different viewpoints. The first two viewpoints (Sects. 4 and 5) deal with basic statistical properties of the free energy (present and original) available on auroral field lines from ion shells. Examples of different types of ion shells with Polar electric field and electron data to give the geophysical context are shown in Sect. 6. Then the behaviour of ion shell free energy and the correlation of ion shells with electron anisotropies and waves is analysed. The paper ends with a summary and discussion.

2 Instrumentation

The Polar satellite has the advantage of having three years of measurements of both ions and electrons, as well as wave electric fields. The results of Janhunen et al. (2003a) have motivated this investigation. The existence of the Polar database makes it possible to systematically investigate correlations between ion shell distributions, electron anisotropy and waves. We use summary Polar/TIMAS ion data from 1996–1998 (Shelley et al., 1995), archived at the NASA Space Science Data Center for identifying and characterising ion shell distributions. The energy range is between 15 eV and 33 keV and the time resolution about 12 s (corresponding to two spin periods). The differential energy flux for the ions is produced in 15° bins for all pitch angles. Ion data exists also after 1998, however, a high-voltage breakdown in TIMAS in 8 December 1998 caused a loss of sensitivity in the data and makes it very challenging to mix data from before and after this date.

During the same time period as for the ion data, i.e. 1996–1998, the wave electric fields in the 1–10 Hz frequency range are available from the Polar Electric Field Instrument, EFI, (Harvey et al., 1995). Polar EFI makes 3-D measurements with a sampling rate of 20 samples per second. We exclude spin axis measurements in this study due to uncertainties in the measurements from the short boom (5 m) in this direction. We make the assumption that the spin axis component of the electric field is negligible in the auroral zone since the spin axis is in the east-west direction here. The parallel and perpendicular wave electric fields will be estimated with the help of the Polar Magnetic Field Experiment (MFE) (Russell et al., 1995).

To investigate the electron anisotropy from the electron distribution function we use the Level-0 Polar HYDRA electron data (Scudder et al., 1995). The energy range of the data is 2 eV–28 keV and the time resolution is about 12 s.

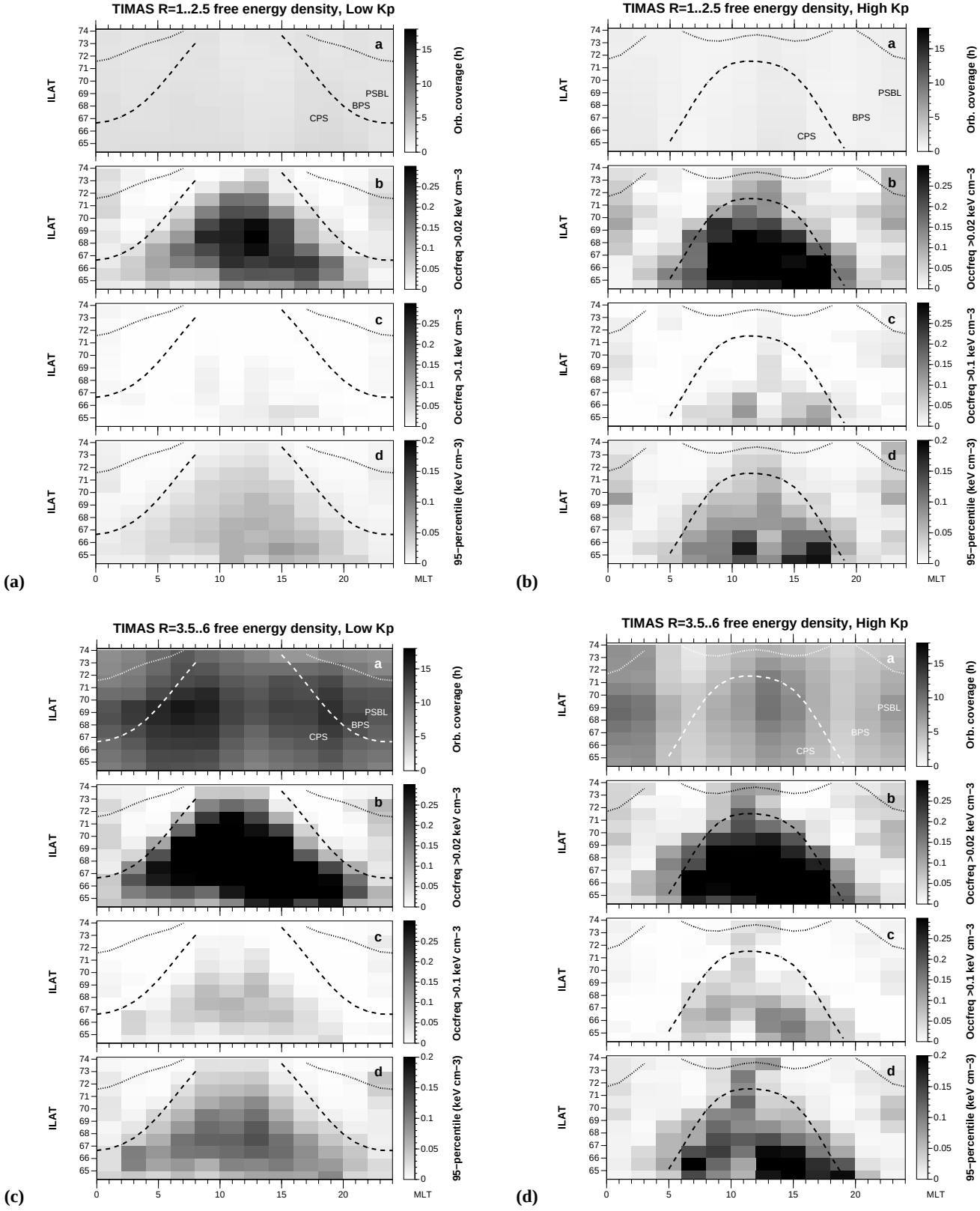

Fig. 1. Ion free energy by Polar/TIMAS as a function of MLT and ILAT for $K_p \leq 2$ (left subplots) and $K_p > 2$ (right subplots). Top plots show include radial distances 1–2.5 R_E, bottom plots 3.5–6 R_E. Orbital coverage in hours in each MLT and ILAT bin **(a)**, fraction of time the free energy exceeds 0.1 keV cm^{-3} **(b)**, fraction of time the free energy exceeds 0.02 keV cm^{-3} **(c)**, 95-percentile of free energy density **(d)**. Some black regions are saturated. The dashed/dotted line is the Holzworth-Meng model auroral oval equatorward/poleward boundary for Q=1.65 (low K_p) and Q=6 (high K_p) (Holzworth and Meng, 1975).

In one event (Fig. 11) we also plot, in addition to EFI spectrogram, a spectrogram above 26 Hz from the plasma wave instrument PWI (Gurnett et al., 1995).

Polar data from the time period 1996–1998 cover the altitude ranges 5000–10 000 and 20 000–32 000 km.

3 Data processing

3.1 Estimate of free energy and downward energy flux from TIMAS

The Polar/TIMAS instrument measures the differential number flux from which the differential energy flux and the distribution function can be obtained by multiplication and division by energy, respectively. In this study we are especially interested in the free energy and the downward total-ion energy flux for ion shell distributions. As described by Janhunen et al. (2003a) we define the free energy of a given distribution function as the difference between the kinetic energy of the original distribution and the kinetic energy of a flattened distribution, which is defined by repeating the following procedure until no positive slopes remain in the flattened distribution data vector f_i, i=1..N:

1. Find the indices i where $f_i < f_{i+1}$, i.e. find the positive slopes. Call these indices i_s, s=1..P. If no indices are found (P=0), the flattening procedure is complete.

2. For each s where $f_{i_s} < f_{i_s+1}$, replace both f_{i_s} and f_{i_s+1} by their arithmetic average (weighted by the cell widths if the discretisation is done in a nonuniformly spaced grid).

The flattening procedure conserves the number of particles (the zeroth moment of the distribution function) and always produces a distribution with no positive slopes. Some more discussion of the prodeduce and an example is given in Janhunen et al. (2003a). The procedure results in an upper limit estimate of the free energy available.

We have checked manually in about 100 events that whenever the free energy parameter as defined here is significant, the reason is always an ion shell distribution. Thus, the free energy density is a good way of automatically finding shell distributions and characterising their strength in a physically meaningful way.

The total-ion downward energy flux is obtained from the differential energy flux by integration over all pitch angles.

3.2 Wave electric fields from EFI and MFE

The EFI electric field was decomposed into parallel and perpendicular components by using spin-resolution (6 s) MFE data. We use frequencies in the 1–10 Hz range. The upper limit is dictated by the EFI instrument which produces 20 samples per second in its usual mode. The wave amplitudes are averaged to the same 12-s time resolution as the particle data.

3.3 Anisotropy from HYDRA

Electron anisotropy is most commonly defined in terms of parallel and perpendicular temperatures. However, in this study we will especially discuss a subrange of electron energy (100–1000 eV) whence it is more convenient to define the anisotropy in terms of density. We define the anisotropy as the partial density corresponding to the part of the electron distribution function from which a symmetrised perpendicular distribution function has been subtracted and the integration in velocity space is carried out between energies 100 eV and 1 keV only. For a detailed discussion on our employed definition of the anisotropy, see Janhunen et al. (2004a), Eqs. 2–4. Statistical results for the MLT-ILAT dependence of the anisotropy of electrons in the energy range 100–1000 eV in the auroral zone can be found in Janhunen et al. (2004a).

4 Free energy of ion shells: dependence on MLT-ILAT, K_p and altitude

To obtain general knowledge about how common and what type of phenomena the ion shell distributions are, we show statistics of their associated free energy in the MLT-ILAT plane in Fig. 1 for low altitudes (R=1–2.5 R_E, top plots) and high altitudes (R=3.5–6 R_E, bottom plots). The left subplots show low K_p ($K_p \leq 2$) and the right subplots show high K_p ($K_p > 2$). Panel (a) shows the orbital coverage in hours, i.e. the number of hours the instrument was measuring in each MLT-ILAT bin. Panel (b) is the occurrence frequency of 12-s data points where the ion free energy exceeds the value 0.02 keV cm^{-3}, panel (c) is the same thing but with a threshold 0.1 keV cm^{-3}, while panel (d) shows the 95-percentile, which is defined as the value such that 95% of the measured values of the free energy are smaller than the plotted value in each MLT-ILAT bin and 5% are larger. Data points when no free energy is found in the distribution are counted as zero. For comparison and for guiding the eye, in each panel, the dashed and dotted lines show the equatorward and poleward boundary of a statistical auroral oval model by Holzworth and Meng (1975). For low K_p, the Q index value needed in the model is set up 1.65 and for high K_p Q=6 is used.

We first discuss features which are common to low and high K_p. It is noteworthy that the occurrence frequency of the free energy exceeding 0.02 keV/cm^{-3} (Fig. 1, panel (b) is highest in the CPS and lowest in the BPS which is seen as almost white. From panel (d), we see that statistically, the ion shells in the CPS are energetic, having values of the free energy density around 0.1 keV/cm^{-3} in 5% of the cases, while lower values (below 0.05 keV/cm^{-3}) of the free energy is found in the PSBL and especially BPS.

Concerning altitude dependence, in the CPS the free energy densities are higher at high altitude than at low altitude. In the BPS and PSBL, however, such a trend is not seen, but the values are uniformly low at both high and low altitudes. The TIMAS time resolution is 12 s, which at low altitude

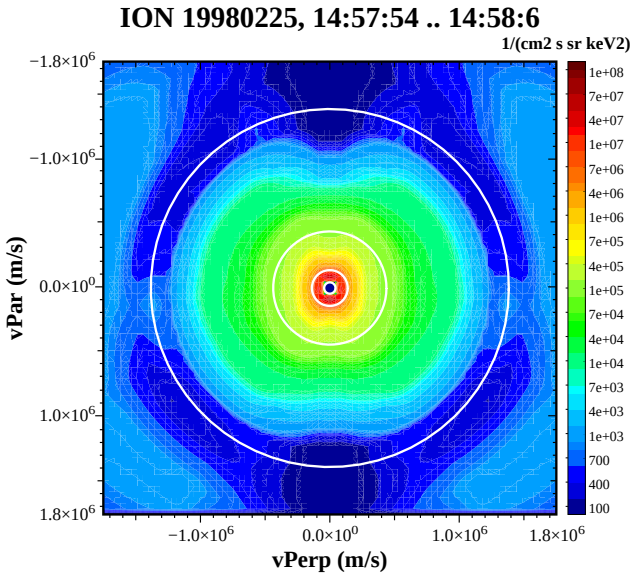

Fig. 2. Example of a CPS ion shell distribution. The quantity shown is the distribution function in units of $\mathrm{cm}^{-2}\,\mathrm{s}^{-1}\,\mathrm{sr}^{-1}\,\mathrm{keV}^{-2}$. Upgoing ions go up and downgoing ions go down in the plot. White circles correspond to energies 10 eV, 100 eV, 1 keV and 10 keV. The shell distribution starts at ∼15 keV and partly falls outside the plot and instrument boundaries in this case. One-count level is 20 times smaller than the shell distribution level, MLT 2, ILAT 67, R=4.4 R_E, n=0.66 cm^{-3}, T=1.9 keV, free energy density 0.15 keV cm^{-3}.

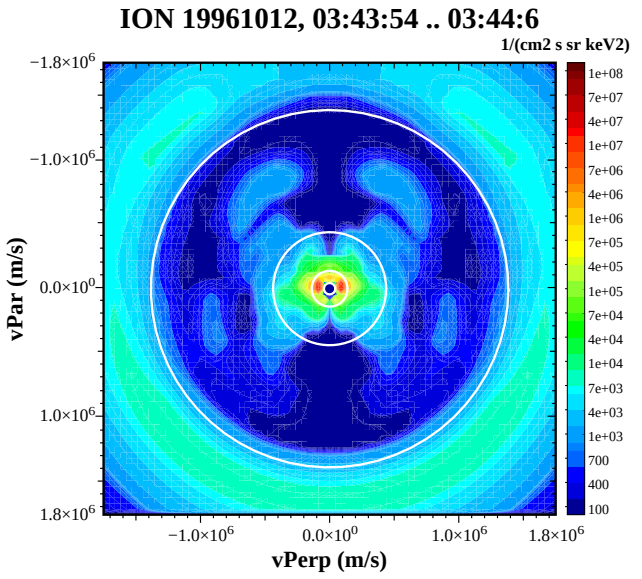

Fig. 3. Example of an event containing a full (i.e. up/down symmetric) ion shell distribution in the PSBL. Format is similar to Fig. 2. One-count level is 200 times smaller than the shell distribution level, MLT 0.9, ILAT 69.5, R=4.3 R_E, n=0.26 cm^{-3}, T=8.6 keV, free energy density 0.64 keV cm^{-3}.

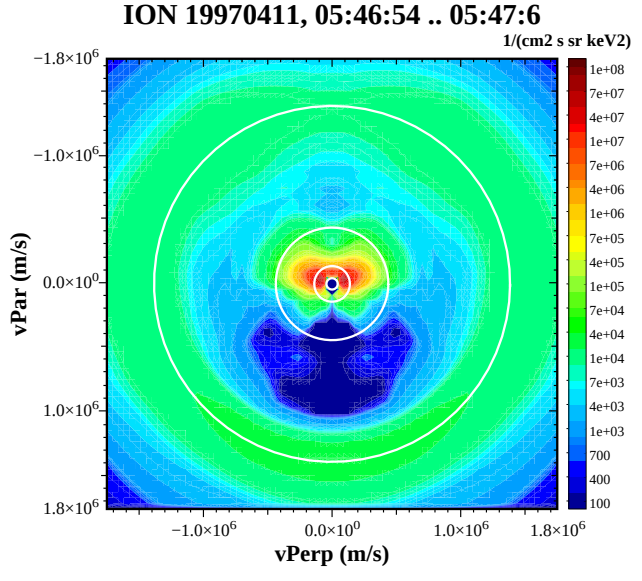

Fig. 4. Example of an event containing a half-consumed shell distribution (i.e. downgoing part is intact but upgoing part has been flattened out). One-count level is 300 times smaller than the shell distribution level, MLT 24, ILAT 68.5, R=4.6 R_E, n=1 cm^{-3}, T=3.4 keV, free energy density 0.44 cm^{-3}.

means that the satellite footpoint moves 20–30 km during each integration period. Some auroral features are smaller than this, so the time resolution may affect the results at low altitude.

The ion shell distributions in the CPS region are thus a common phenomenon. From looking at the individual CPS events one discerns that the ions are typically energetic (above 15 keV), and the distributions are stable, i.e. their free energy is not consumed. A typical example of an ion shell in the CPS is shown in Fig. 2. We think that CPS ion shells are often associated with ion spectral gaps and "nose" structures (McIlwain, 1972; Buzulukova et al., 2002) and monoenergetic ion drop-offs (Shirai, et al., 1997).

Ion shells in the PSBL (and BPS, whenever they occur) usually have lower ion energies than in the CPS, usually below 10–15 keV (Fig. 3). For midnight MLT (22–02) one can see in Fig. 1, panels (b–d) that the occurrence frequency of auroral ion shells is highest in latitudes corresponding to the part of the auroral zone adjacent to the polar cap (from ILAT ∼68). Probably these ion shells originate from the PSBL and we will therefore refer to these ion shells as PSBL ion shells. In some events one sees ion shells also between the PSBL and the CPS, i.e. in the BPS; this may be either a genuine effect or be caused by auroral oval motion while the satellite is crossing it.

We now discuss the K_p differences seen in Fig. 1. The most evident observation is that the boundary of the dark and light regions (CPS and BPS) moves with K_p very similarly to the statistical oval equatorward boundary (dashed line). Otherwise, the energy densities increase with K_p overall. In the PSBL, the free energy density is somewhat higher for high K_p and it is spread more uniformly over the MLT sectors

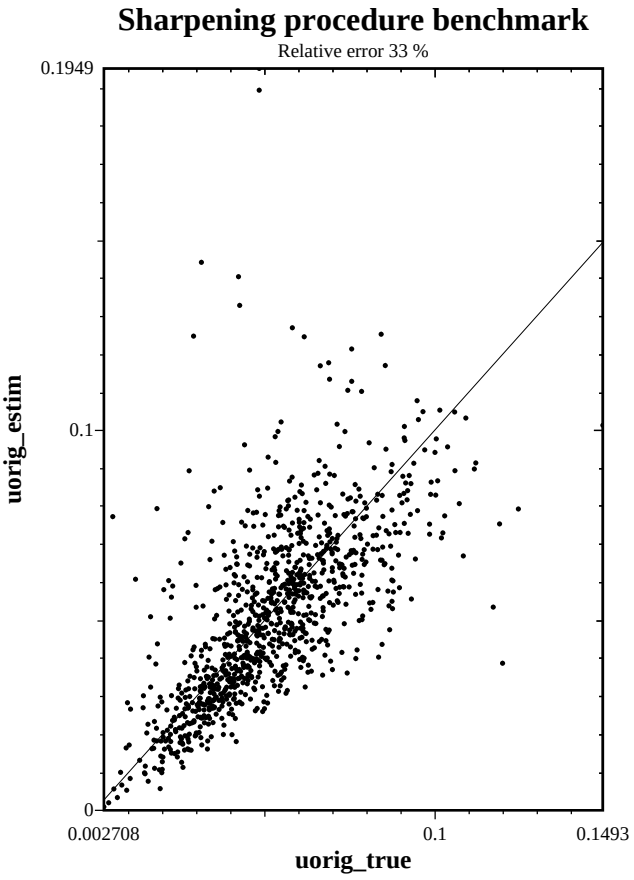

Fig. 5. Benchmark result of the sharpening procedure in a random ensemble of 1000 distributions. The horizontal axis is the true free energy of the original distribution and the vertical axis is the free energy found by the sharpening procedure.

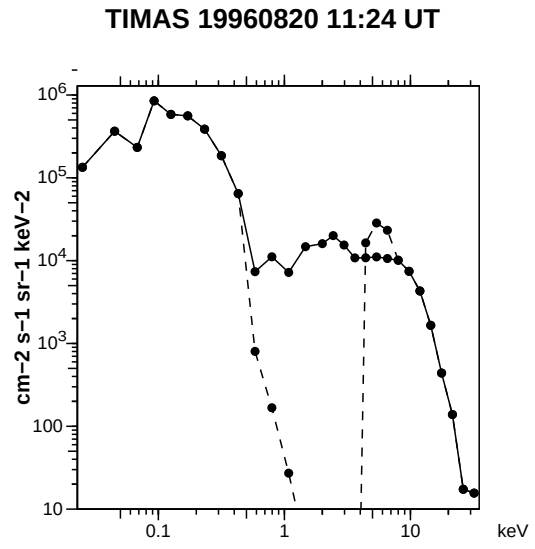

Fig. 6. Application of the sharpening procedure to TIMAS data ($0--30°$ pitch angle) taken on 20 August 1996, 11:24 UT (MLT 3.4, ILAT 69, R 4.1 R_E) in the Northern Hemisphere. Solid line is the original distribution and dashed line the sharpened version. A plateau exists between 1 and 10 keV that the procedure has found and replaced by a shell distribution, conserving the number of particles. The plateau is not completely smooth in this case, but this does not harm the sharpening procedure.

20–04, while for low K_p it is more concentrated in the midnight sector (22–02 MLT).

Typically, many of the ion shell distributions in the PSBL and especially BPS (for 1–6 R_E) are partly flattened out. As an example, Fig. 4 shows a half-consumed ion shell: the downgoing part is an ion shell but the upgoing part is nearly a plateau. A natural idea is that the plateau in the upgoing part is due to wave-particle interactions which have consumed the free energy of the downgoing ion shell. In the case of a half-consumed ion shell the consumption process should occur below the measurement point.

5 Consumed free energy of plateau distributions

If the ion shell distribution free energy is consumed by wave-particle interactions, a plateau is expected to be left at and near the energy range where a positive slope existed before. Plateaus in the ion distribution are therefore possible markers of free energy that has existed in the original distribution and that was subsequently consumed. If it is possible to reconstruct the original distribution from the plateaued one approximately, it is then possible to estimate its original free energy. In this section we define an automatic algorithm for doing this and validate it by applying it to an ensemble of synthetic distributions whose original free energy is known by construction. Finally, by subtracting the free energy from the estimated original free energy we obtain the part of the energy that was consumed. The consumed energy density is shown at the end of the section in statistical results where we show the MLT-ILAT dependence on altitude and K_p.

5.1 Sharpening procedure

Consider a 1-D distribution function represented by N discrete data points f_i, i=1..N (N=28 for TIMAS). In the algorithm we take f to be the logarithm of the distribution function. The procedure takes f as input and produces a "sharpened" version f_s which has a plateau replaced by the corresponding sharp shell distribution. Assume that there are indices i_1, i_2, i_3 and i_4 ($1 \le i_1 < i_2 < i_3 < i_4 \le N$) defining a left negative slope region $i_1..i_2-1$, a candidate plateau or positive slope (POPS) region $i_2..i_3$ and a right negative slope region $i_3+1..i_4$. Define their mean slopes by

$$s_L = (f_{i_{2-1}} - f_{i_1})/(i_2 - i_{1-1}) \quad (1)$$

and

$$s_R = (f_{i_4} - f_{i_{3+1}})/(i_4 - i_{3-1}). \quad (2)$$

We require that both slopes are negative, i.e. that $s_L < 0$ and $s_R < 0$, and that the length of both negative slope regions is three datapoints, i.e. $i_2 - i_1 = i_4 - i_3 = 3$. By using simulated

cases we determined that three is the optimal number in our case. For the candidate POPS region, its mean slope is defined as:

$$s = (f_{i_3} - f_{i_2})/(i_3 - i_2). \quad (3)$$

We set the following inequality requirement for the POPS region:

$$\min(s, f_{i_{2+1}} - f_{i_2}, f_{i_3} - f_{i_{3-1}}) \geq 0.2 \max(s_L, s_R). \quad (4)$$

This requirement means that both POPS region overall slope s, as well as its starting slope $f_{i_{2+1}} - f_{i_2}$ and ending slope $f_{i_3} - f_{i_{3-1}}$ must be large enough; in particular, if all are non-negative, the inequality is always satisfied since s_L and s_R were already above required to be negative.

We start searching for a POPS region satisfying the above requirements first by trying the longest possible POPS region that fits into the data vector, together with the required left and right negative slope regions. If a good POPS region is not found, the length is decreased by one and the search is reinitiated. Within each length, the search propagates from high towards low energies. The first POPS region satisfying the above requirements terminates the search.

If and when a good POPS region is found, linear expressions of the form $f(v)=a+bv$ are fitted to the left and right negative slope regions around the POPS region by finding a and b for each. Notice that since f is the logarithm of the distribution function, these expressions are actually exponentials in physical space. These expressions are extrapolated inside the POPS region. The cutoff velocity value where the left fit suddenly transforms to the right fit is defined by requiring that the number of particles (first moment of f, weighted by v^2 in the 3-D case) does not change when the POPS region is replaced by the fitted expressions. The proper fitted expressions are finally evaluated in the integral fashion (i.e. means are computed over the grid cell instead of using pointwise values) inside the POPS region and the obtained values form the sharpened vector f_s. If no good POPS region is found, f_s is set equal to f. The original free energy is defined to be the free energy of f_s, where the free energy is calculated by the flattening procedure of Sect. 3.1. By construction, the original free energy is always at least as large as the free energy of f defined in Sect. 4 and in case a good POPS region was found, it is larger.

5.2 Validation

We validate the method by generating an ensemble of 1000 random distributions. We superpose two Maxwellians with different temperatures. The temperatures and densities of both are taken from random numbers and vary within reasonable limits, corresponding to typical distributions seen in the magnetosphere. The hotter Maxwellian is turned into a shell distribution by taking a cutoff point, below which the values are set to a smaller value. The cutoff point and the smaller value are also taken from random numbers. Ten percent of Gaussian noise is added to each data point of the result. The resulting distribution f_{orig} is then run through the flattening procedure (Sect. 3.1) to mimic waves using the free energy of the shell distribution. The flattened version is mixed with a random mixing ratio with the original distribution to simulate partial free energy consumption. The resulting distribution f is the one that we imagine is measured by the virtual instrument and is fed into the sharpening procedure defined above. The algorithm produces the sharpened version f_s which should approximate f_{orig}. Comparison of the free energies of f_s and f_{orig} measures the goodness of the sharpening procedure.

The benchmarking results are shown in Fig. 5. The horizontal axis is the known free energy of f_{orig} and the vertical axis is the free energy of the sharpened distribution f_s, normalised to the total kinetic energy of the distribution function. It can be seen that the sharpening procedure does a good job on simulated data, since the data points cluster nicely around the $f_s = f_{\text{orig}}$ line. We define the relative error of each data point by

$$\epsilon = \frac{|u(f_s) - u(f_{\text{orig}})|}{\min(u(f_s), u(f_{\text{orig}}))}, \quad (5)$$

where $u(f)$ denotes the free energy of f found by flattening. In the simulation ensemble, the average ϵ is 33%.

In Fig. 6 we show an example of the sharpening procedure applied to TIMAS data. A plateau between 1 and 10 keV energies exists in this case, which the program finds and replaces by a shell distribution having the same number of particles. The shell cutoff energy is about 4 keV.

5.3 Consumed energy dependence on MLT-ILAT, K_p and altitude

Previously, we discussed the statistical distribution of the free energy density $u(f)$ (Fig. 1). For the sharpened version f_s we now define the consumed energy density

$$u_{\text{cons}} = u(f_s) - u(f), \quad (6)$$

i.e. u_{cons} is an estimate of the energy that was consumed when the distribution was partly or completely plateaued by wave-particle interactions. For pure shell distributions and for quasi-Maxwellian (non-plateaued) distributions, u_{cons} is zero, but it is nonzero for plateau distributions and partly flattened-out shell distributions. Figure 7 shows the statistical distribution of u_{cons}. The meaning of the panels and their scaling is identical with Fig. 1, except that the quantity shown is u_{cons} instead of $u(f)$.

We make the following observations concerning the consumed energy density from Fig. 7. There is not much altitude dependence in the BPS/PSBL region, although in the CPS, the consumed energy is higher at high altitude than at low altitude. This trend is similar to what was seen for the free energy earlier (Fig. 1). The CPS region (mostly black in panels (b) of Fig. 7) moves equatorward for increasing K_p, in a way which is in good agreement with the equatorward boundary of the Holzworth-Meng oval model (dashed line). This is also similar to the free energy density behaviour (Fig. 1).

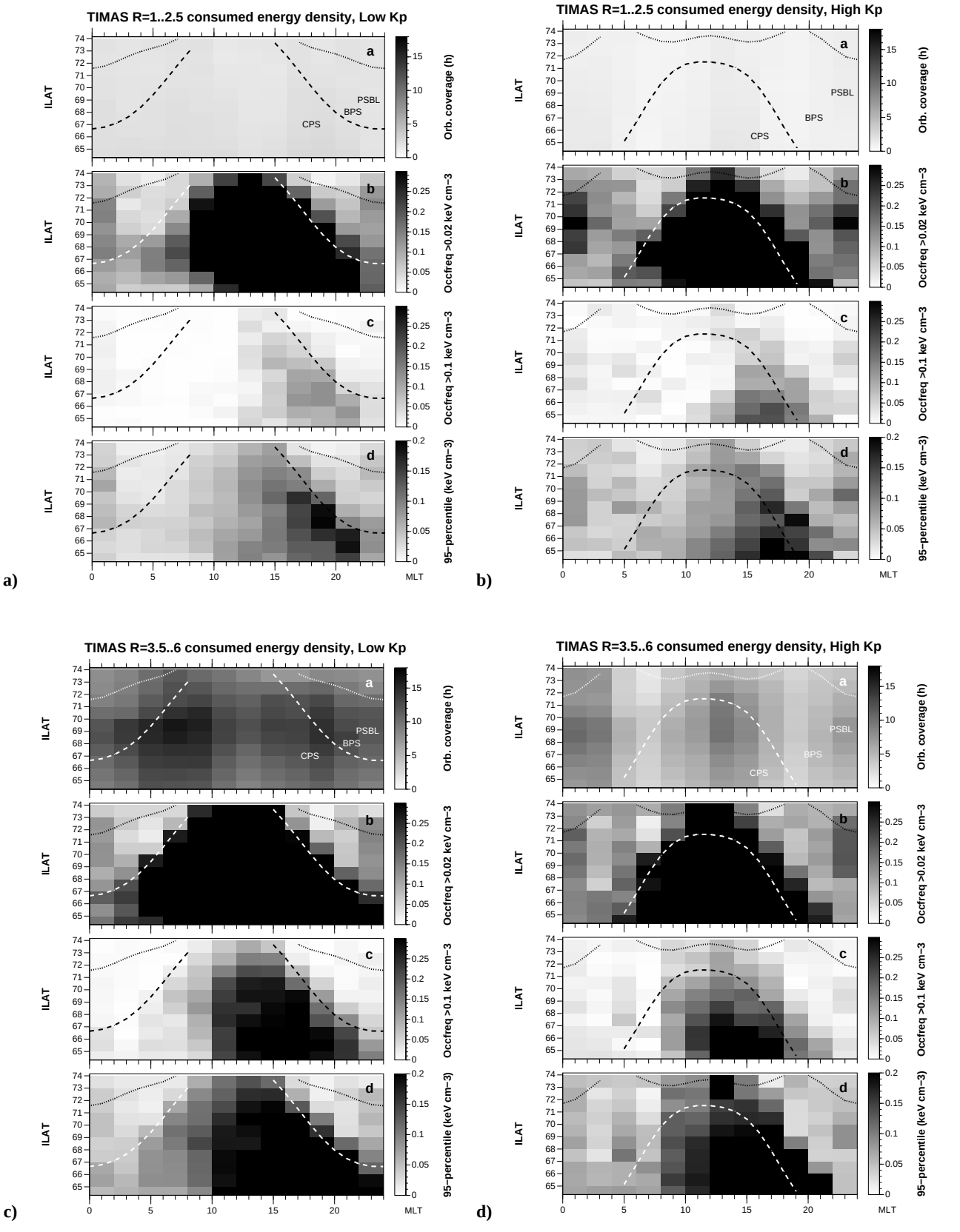

Fig. 7. Same as Fig. 1 except that now the quantity shown is the consumed free energy u_{cons}, Eq. (6).

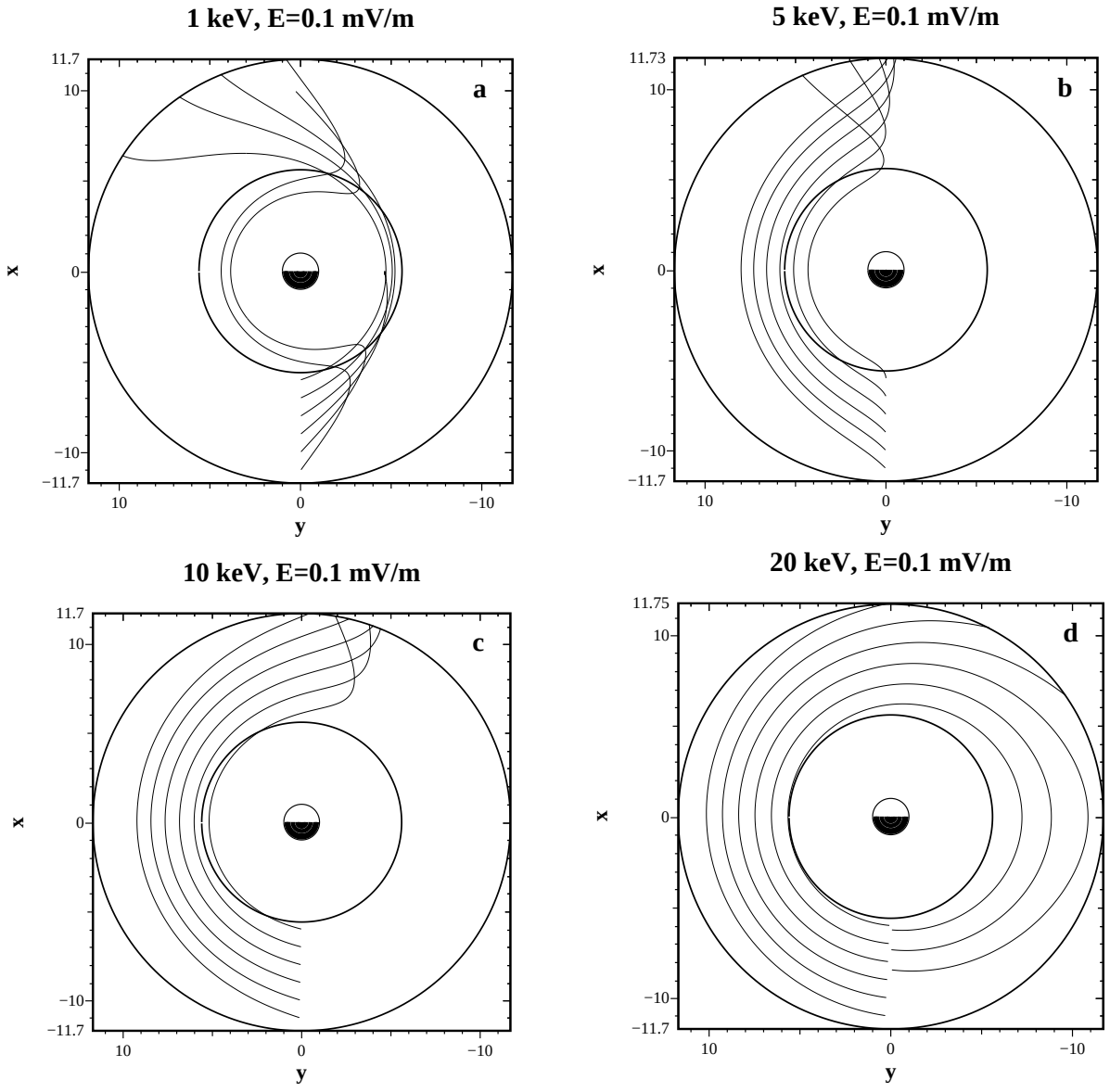

Fig. 8. Drift paths of equatorial protons launched from MLT 24 for energies 1 keV **(a)**, 5 keV **(b)**, 10 keV **(c)** and 20 keV **(d)**. Circles corresponding to 65 and 73 ILAT are drawn, approximately corresponding to the range of data. Dipole magnetic field and a uniform duskward electric field of 0.1 mV/m are assumed.

Comparison of the free energy (Fig. 1) and the consumed energy statistics (Fig. 7) shows that the mean auroral oval between the dashed and dotted lines (BPS and PSBL) contains significant consumed energy (Fig. 7), although we saw earlier that it does not contain so much free energy on the average at radial distances below 6 R_E (Fig. 1). The BPS is seen in the free energy plots (Fig. 1) as an almost empty region between two enhanced regions, CPS and PSBL (at the PSBL, the enhancement is much smaller than in CPS). But for the consumed energy density (Fig. 7), a contrast between BPS and PSBL is no longer seen. We suggest that this is because the free energy is introduced at the PSBL in the form of VDIS shell distributions and is mostly consumed in the BPS, leaving behind plateau distributions.

We now discuss how to understand that u_{cons} is enhanced at low latitudes in the postnoon sector, but not so much in the prenoon (Fig. 7). In Fig. 8 we show drift paths of equatorial plane protons for different energies (1, 5, 10 and 20 keV), assuming a dipole magnetic field (for similar calculations, see, e.g. Ejiri (1978)). The particles are launched at MLT 24. The drifts taken into account are the $E\times B$ drift and the gradient drift, the curvature drift is zero for equatorial particles. In the $E\times B$ drift, the corotation field and a constant duskward electric field of 0.1 mV/m magnitude are included. The 1 keV protons (panel (a)) show competition between the corotation drift and the gradient drift since they propagate eastward or westward, depending on their initial condition. At 5 and 10 keV (panels (b) and (c)) the particles drift westward due to

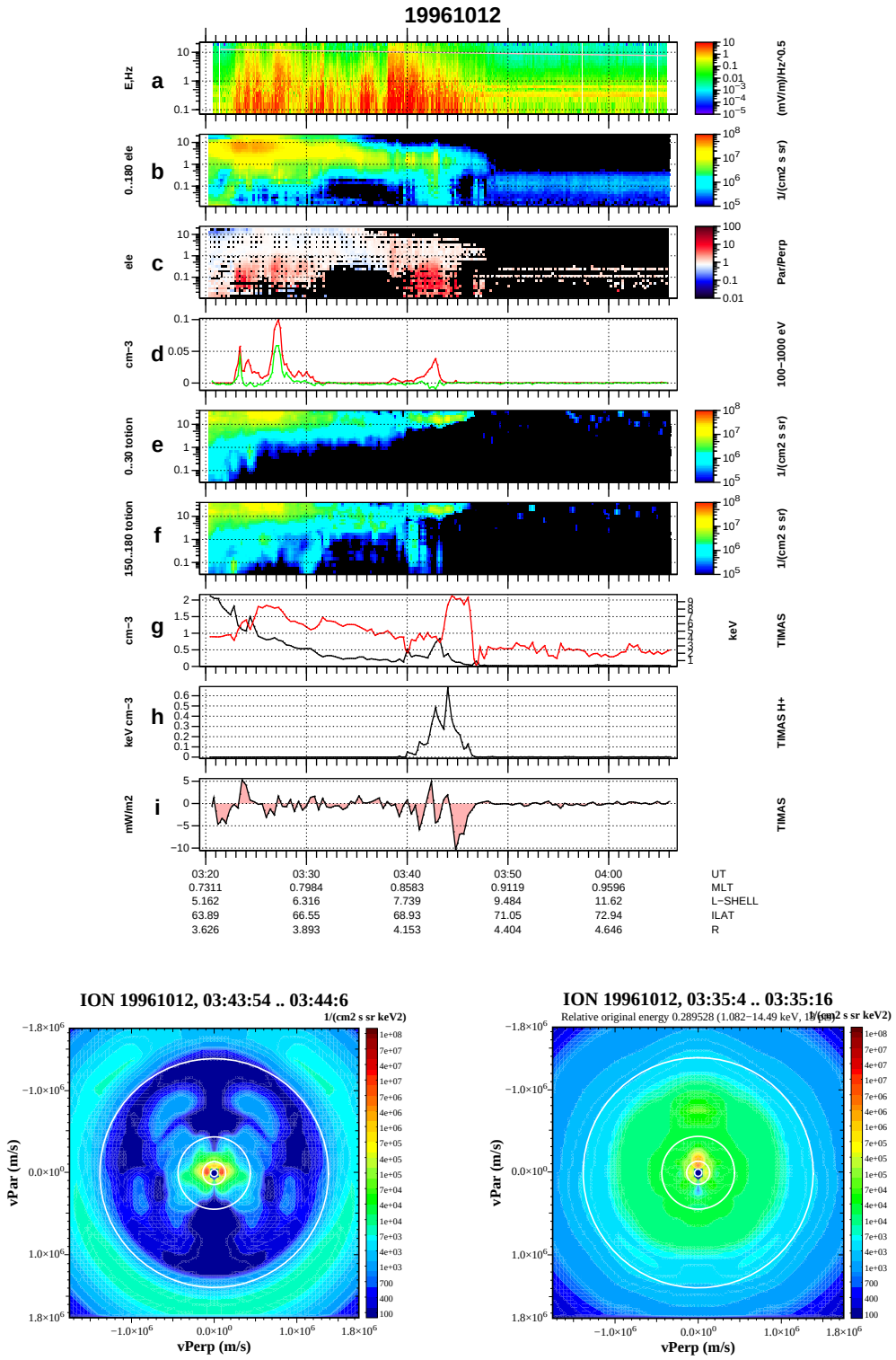

Fig. 9. Polar data for 12 October 1996, 03:20–04:08 UT. Example of an event containing a full (i.e. up/down symmetric) shell distribution. Upper subfigure: **(a)** EFI electric wave amplitude spectrogram, **(b)** electron differential energy flux spectrogram from HYDRA including all pitch angles **(c)** ratio of parallel to perpendicular electron distribution function from HYDRA, red regions signifying parallel electron energisation, **(d)** parallel minus perpendicular electron distribution function integrated between 0.1 and 1 keV, i.e. the anisotropic density (red) and up minus down parallel component, positive meaning upgoing electrons (green), **(e)** total ion distribution function from TIMAS for 0–30° pitch angle, i.e. downgoing, **(f)** same for antiparallel (upgoing) ions, i.e. 150–180°, **(g)** ion density (black) and temperature (red, scale on the right) computed by integration from TIMAS total ion distribution function, **(h)** free energy density in TIMAS ion distribution, **(i)** energy flux estimated from the free energy, positive upward. Left lower subfigure: the full shell distribution in the PSBL, with similar format as in Fig. 2, one-count level 200 times smaller than shell level. Right lower subfigure: distribution function at 03:35 UT in the BPS, where a Maxwellian with plateauing tendency is seen, one-count level 30 times smaller than shell level.

the gradient drift, but exit from the magnetosphere near noon due to the duskward electric field. At 20 keV (panel (d)) the gradient drift is strong enough to keep the particles trapped so that they also propagate to the morningside. In TIMAS data, the intact, unconsumed shell distributions at low latitudes (CPS) are usually at high energies (more than 15 keV). As seen in panel (d), such protons are trapped and are found at both prenoon and postnoon sectors. This is probably the reason why the free energy density plots (Fig. 1) are almost symmetrical in MLT about noon. The situation is different for the plateau distributions corresponding to the quantity $u_{\rm cons}$ shown in Fig. 7, however, these protons are usually at somewhat lower energies ($\sim$2–10 keV). According to Fig. 8, such protons exist only in the postnoon sector; thus, this explains why $u_{\rm cons}$ is enhanced at subauroral latitudes in the afternoon sector but not in the morning sector.

6 Partly consumed PSBL and BPS ion shells

When manually looking through individual PSBL and BPS shell distributions we have already mentioned that the ion shells often seem to be just partly shell-like, i.e. the ion shells have been partly consumed. To quantify this in yet another way, we calculate the free energy density (Sect. 3.1) separately for upgoing and downgoing parts of the distribution and compare them. If the amount of free energy is equal in both directions, the distribution is a full ion shell. If the downgoing free energy is about two times larger than the upgoing one, we say that the shell is 1/4-consumed. If there is free energy only in the downgoing direction, we say that the shell is half-consumed, or, if a visual inspection shows that the "rim" of the shell exists only for downgoing and parallel-dominated particles, it can be 3/4-consumed. Other types of partial shells not fitting to this classification scheme can be thought of, but are not often seen in data.

We now present example events where these different types of shells are seen in their geophysical context. We start from the simplest type which is a full ion shell. In Fig. 9 we show Polar data from several instruments (upper subfigure), together with the TIMAS distribution function (lower subfigures) portraying a full ion shell. Panel (a) is an EFI wave spectrogram showing electric wave activity. Panel (b) is the electron differential energy flux spectrogram from HYDRA, including all pitch angles. Panel (c) is a measure of electron anisotropy, the quantity shown is the measured differential energy flux in the parallel direction divided by the measured differential energy flux in the perpendicular direction (Janhunen et al., 2004a). $T_\parallel > T_\perp$ electron anisotropies are seen as red in panel (c). Panel (d) shows the anisotropic part of the density for middle-energy (100–1000 eV) electrons only in red and the up minus down anisotropy in green. The quantities shown in panels (c) and (d) are defined more exactly in Janhunen et al. (2004a). Panels (e) and (f) are spectrograms for down and upgoing TIMAS ions, respectively. The quantity plotted is the differential energy flux for all ion species summed together. Panel (g) shows the density and temperature calculated from TIMAS total ion data. Panel (h) is the free energy density in keV cm^{-3} for TIMAS protons, computed by the flattening method of Sect. 3.1. Finally, panel (i) shows the parallel energy flux for all TIMAS ions (positive upward). The energy flux has been mapped to the ionospheric plane, i.e. multiplied by the ratio of ionospheric versus local magnetic field and is expressed in mW m^{-2}. The left subfigure of Fig. 9 shows a typical full shell distribution in the PSBL and the right subfigure a typical, almost Maxwellian, BPS distribution with some plateauing in the few keV energy range, with no shell distribution. A full shell distribution indicates that the shell distribution free energy is currently not being consumed either at, below or above the observation point.

Figure 10 shows an example of a 1/4-consumed shell. Like the previous full shell example (Fig. 9), this shell also occurs in the PSBL with a clear VDIS. This shell has a rather strong superposed upgoing ion beam which covers a broad range of energies. The shell is plateaued in about a $\pm 45^\circ$ wide cone in the upgoing part, hence it is 1/4-consumed. Alternatively, one could interpret the distribution so that it is a full shell where a superposed ion beam extends up to the shell energy. The valley (or hollow) at lower energy than the shell rim is deepest in the downgoing direction (zero pitch angle) and becomes more filled for increasing pitch angles. Our interpretation is that in this case the observation point is well above the region where waves consume the free energy.

A half-consumed PSBL/VDIS shell is shown in Figure 11. There is a superposed ion conic extending to $\sim$1 keV energy. Such a wide bowl-like conic is indicative of wave-induced perpendicular ion energisation only slightly below the observation point (Klumpar et al., 1984). The upgoing part of the shell is almost consumed (plateaued) in this case. The right lower subplot shows the simultaneous electron distribution function. Middle-energy electrons are energised in the parallel direction (see also panels (c) and (d) in the upper subplot). The association with middle-energy electron anisotropies (Janhunen et al., 2004a) is very typical to half-consumed shells. One interpretation is that the satellite is just on the top of the region where waves consume energy. The ion bowl is consistent with this interpretation, since at least, if the waves are ion Bernstein waves, they can both increase the parallel energy of the electrons and the perpendicular energy of the ions (Janhunen et al., 2003a).

A 3/4-consumed shell example is shown in Fig. 12. The event is similar to the previous one (Fig. 11), except that the unconsumed part of the shell is now less than 2π solid angle. One interpretation is that the observation point is inside the region where the waves consume energy.

A shell distribution whose downgoing part is stronger than the upgoing part but with no indication of plateauing is shown in Fig. 13. This distribution can be explained by a high-altitude source which is intensifying in time.

We now mention some properties of ion shells and related Polar parameters that we have learned by looking at many plots similar to those shown in Figs. 9–13.

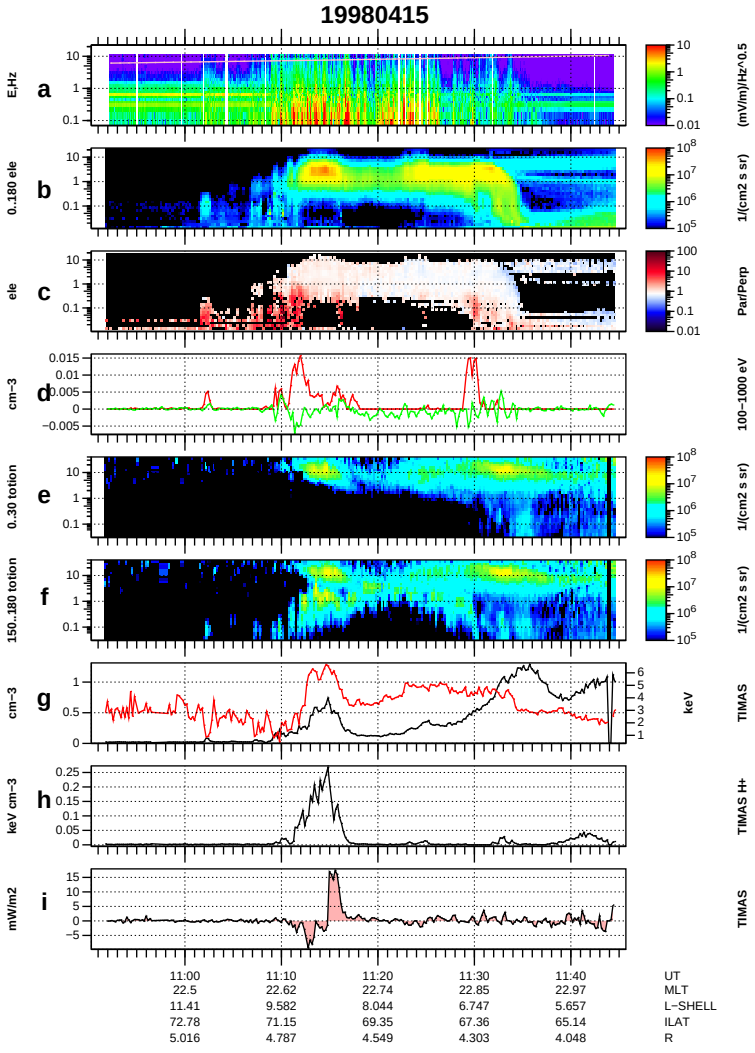

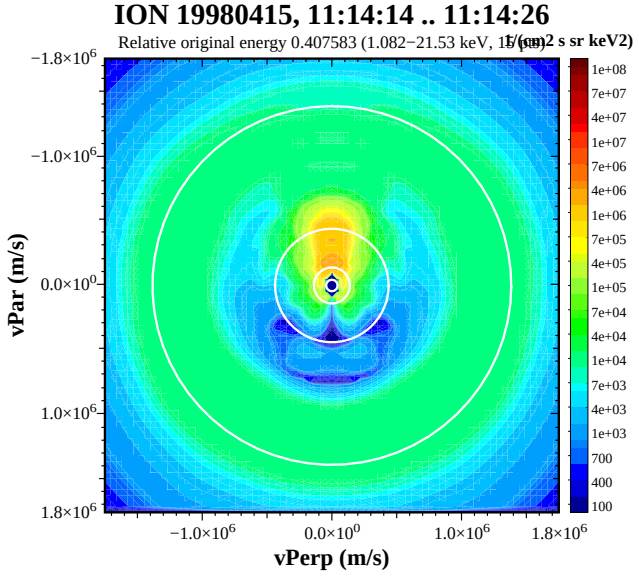

Fig. 10. Example of an event containing a 1/4-consumed shell distribution (i.e. downgoing part is intact but small pitch angles of upgoing part have been flattened out). Format is similar to Fig. 2. One-count level 100 times smaller than shell level.

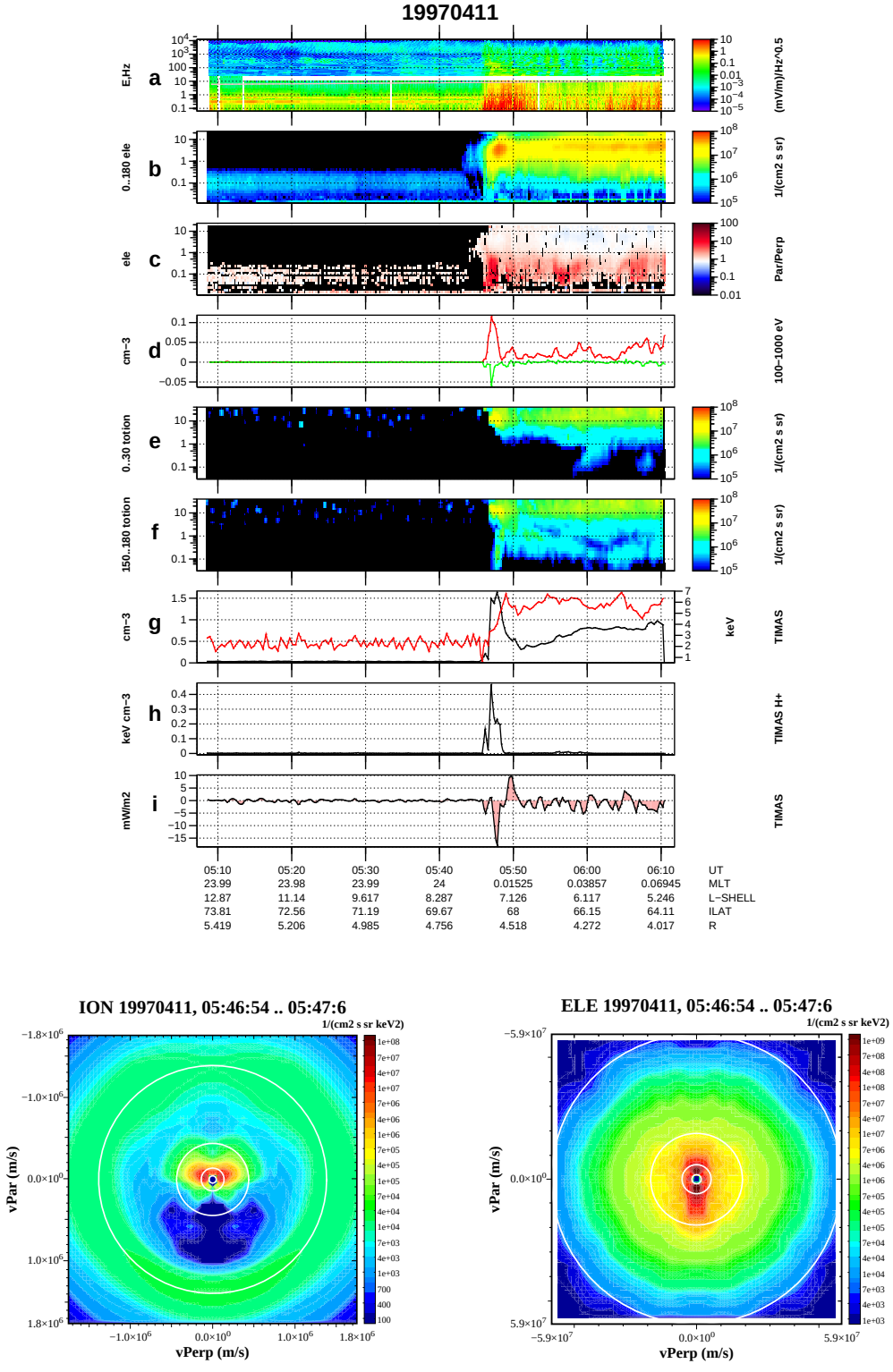

Fig. 11. Example of an event containing a half-consumed shell distribution (i.e. downgoing part is intact but upgoing part has been flattened out). In all PSBL events we have looked at there is always an upgoing ion beam embedded within the shell. Format is similar to Fig. 9 except that in panel (a), PWI wave data spectrogram has been added at frequencies 26 Hz–10 kHz in addition to the standard EFI spectrogram below 10 Hz. One-count level is 300 times smaller than shell level.

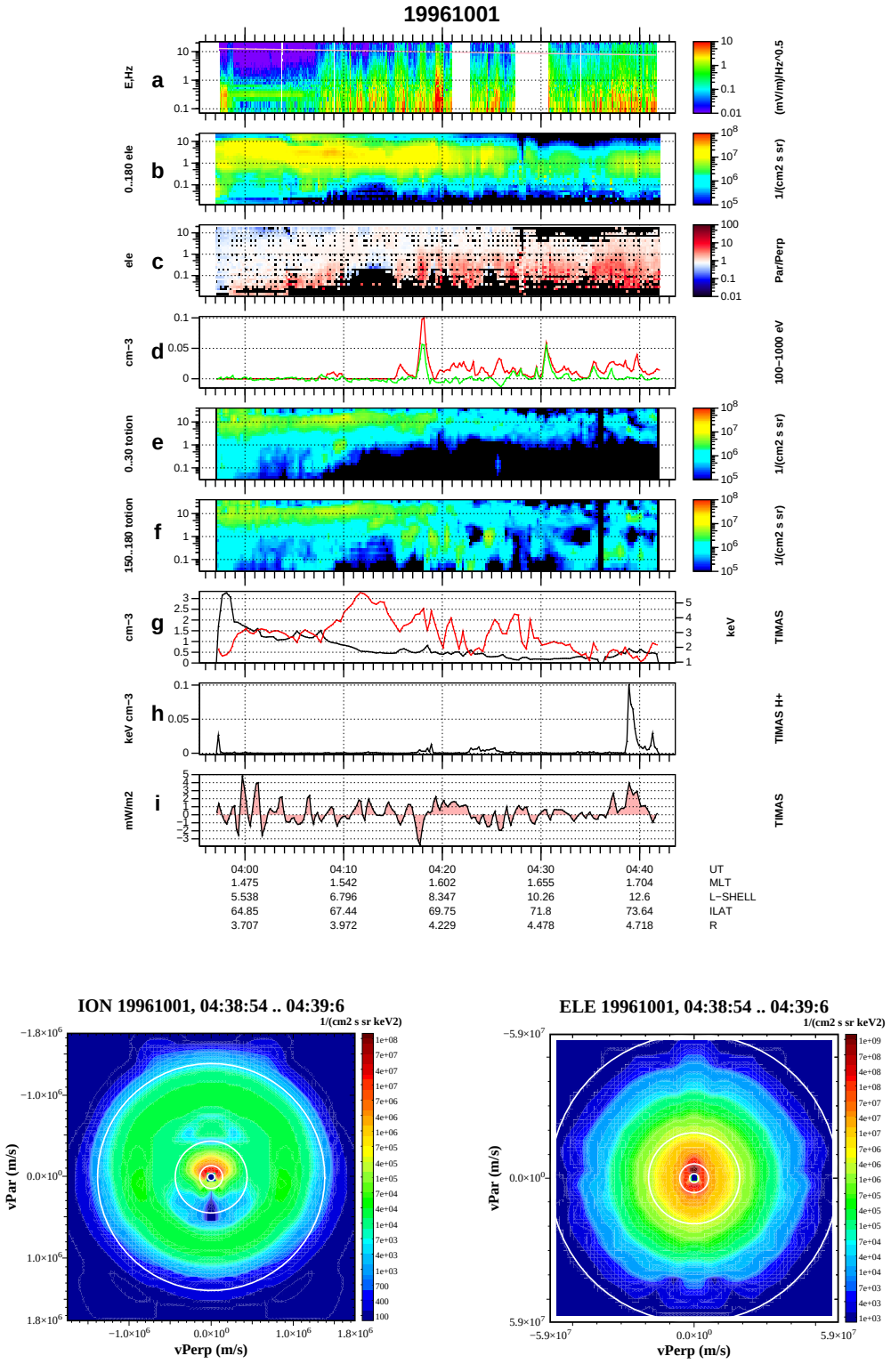

Fig. 12. Example of an event containing a 3/4-consumed shell distribution (i.e. only the small pitch-angle part of the downgoing part is intact, the rest of the distribution has been flattened out). In all PSBL events we have looked at there is always an upgoing ion beam embedded within the shell. Format is similar to Fig. 9. One-count level is 100 times smaller than shell level.

In the auroral region, usually the largest ion distribution free energy density occurs near the polar cap boundary, i.e. in the PSBL. This will be studied in Sect. 7 below.

Whenever there is an ion shell (full shell or partly consumed shell), there is always an upgoing ion beam or ion conic (seen in panel (f) in the upper subfigures and near the centre of the distribution function subfigures). This is not too surprising since upflowing ion beams are common everywhere in the auroral region (Janhunen et al., 2003b), but it is interesting that among those several hundred distribution functions that we have looked at, there is not even one counterexample to this rule. It is possible that the ions are perpendicularly energised by the waves driven at lower altitude by the shell distribution. Related to this, it was recently shown that low energy (<100 eV) ion outflows occur often in the PSBL (Malingre et al., 2000). Another interesting fact that we mention without showing a plot is that if one separates the counts in hydrogen and oxygen, one finds that the shell distribution is almost always purely hydrogen, whereas the upgoing beam or conic is a mixture of hydrogen and oxygen.

When PWI SFRA data are available, one finds that broad-band features seen in EFI below 10 Hz usually correlated rather well with higher frequency broad-band features in PWI frequencies (26 Hz–10 kHz). An example is seen in Fig. 11. When considering shell distribution correlation with wave activity we use the usually available EFI 1–10 Hz frequency range, but we stress that this does not necessarily imply that the waves physically coupling to the shell distribution are found below 10 Hz. It has been shown that ion shell distributions can drive unstable ion Bernstein waves in, say, 50–500 Hz frequency range (Janhunen et al., 2003a).

Electron anisotropies in the auroral region usually occur in middle energies (100–1000 eV). This is seen clearly in Figs. 9 and 11. The correlation of middle-energy electron anisotropies with the auroral zone (BPS) has recently also been shown statistically (Janhunen et al., 2004a).

The downgoing ion energy flux in, for example, half-consumed ion shell distributions (panel (g)) is often $\sim$15 mW m^{-2} when mapped to the ionospheric plane (e.g. in Fig. 11). Energetically, this is already enough to power ordinary electron auroral arcs. A marginally visible electron arc is 1 mW m^{-2}, a bright arc 10 mW m^{-2} and a very bright substorm-related aurora can exceed 100 mW m^{-2}.

There is often a gap in the high-energy ions after the VDIS ion shell feature of the PSBL (e.g. Fig. 9, 03:32–03:40, Fig. 10, around 11:20, Fig. 11, 05:50–05:55), as pointed out by Bosqued et al. (1993b). This could be explained as the gap between the highest latitude and the next-highest latitude ion beamlets (Fig. 17 of Ashour-Abdalla et al., 1993; see also the Plates of Bosqued et al., 1993b, for simulated low-altitude ion precipitation energy flux latitudinal profile). It was concluded by Bosqued et al. (1993b), using low-altitude observations, that when the VDIS are observed, the most poleward electron inverted-V arc is usually displaced 1–2° from the VDIS, i.e. that there is a gap between them. In the light of ion shell distribution free energy feeding auroral arcs, this might happen because the VDIS can be observed at low altitude only if its free energy is not consumed, i.e. when there is no arc: the next chance to consume the energy comes at the next bounce of the ions, which is where the most poleward inverted-V arc appears.

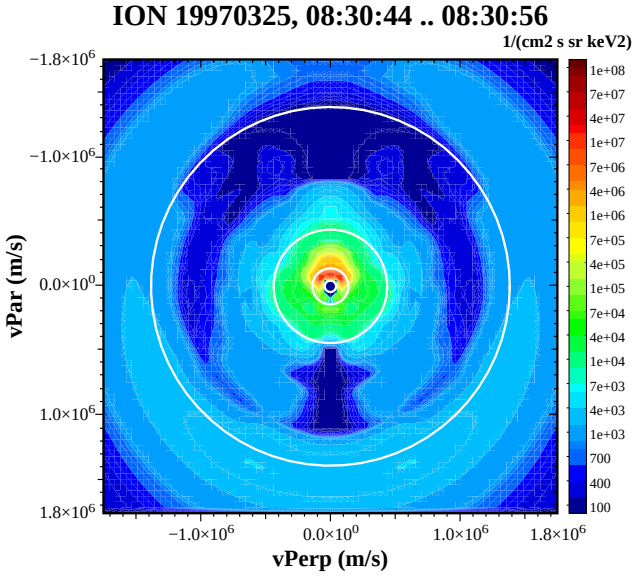

Fig. 13. Example of an event containing a full ion shell distribution whose downgoing part is stronger than the upgoing one, indicating a high-altitude source process which is becoming stronger with time. Format similar to 9. One-count level is 40 times smaller than shell level, MLT 0.9, ILAT 69, R=4.8 R_E, n=0.15 cm^{-3}, T=4.3 keV, free energy density 0.08 keV cm^{-3}.

7 Shell, wave activity and electron anisotropy correlation

We have already discussed the correlation between partly consumed shells, wave activity and electron anisotropy but will here discuss it in another form. In Fig. 14 we show summary plots of ten Polar auroral zone crossings having half-consumed ion shell distributions with significant free energy densities. Each panel in the figure shows one auroral crossing, with the horizontal axis being the invariant latitude. The black line in each panel is the free energy density of the TIMAS ion distribution with the scale on the left. The red line is the middle-energy electron anisotropy (same as panel (c) in Fig. 9) with the scale on the right. The green line is the EFI electric wave amplitude in the 1–10 Hz frequency range, averaged in 12-s blocks. The wave amplitude curve is normalised to its maximum, but the maximum value (mV/m) is written in each panel, as is also the maximum downward TIMAS ion energy flux (mW m^{-2}). The maximum for the downward energy flux is taken over those datapoints whose free energy density exceeds 0.02 keV cm^{-3}; usually the maximum downward energy flux occurs near the maximum free energy density (black curve). In addition, each panel contains information about the date, whether Polar is moving to the left (L) or right (R) in the plot and the UT hour, MLT and radial distance R of the centre of the crossing.

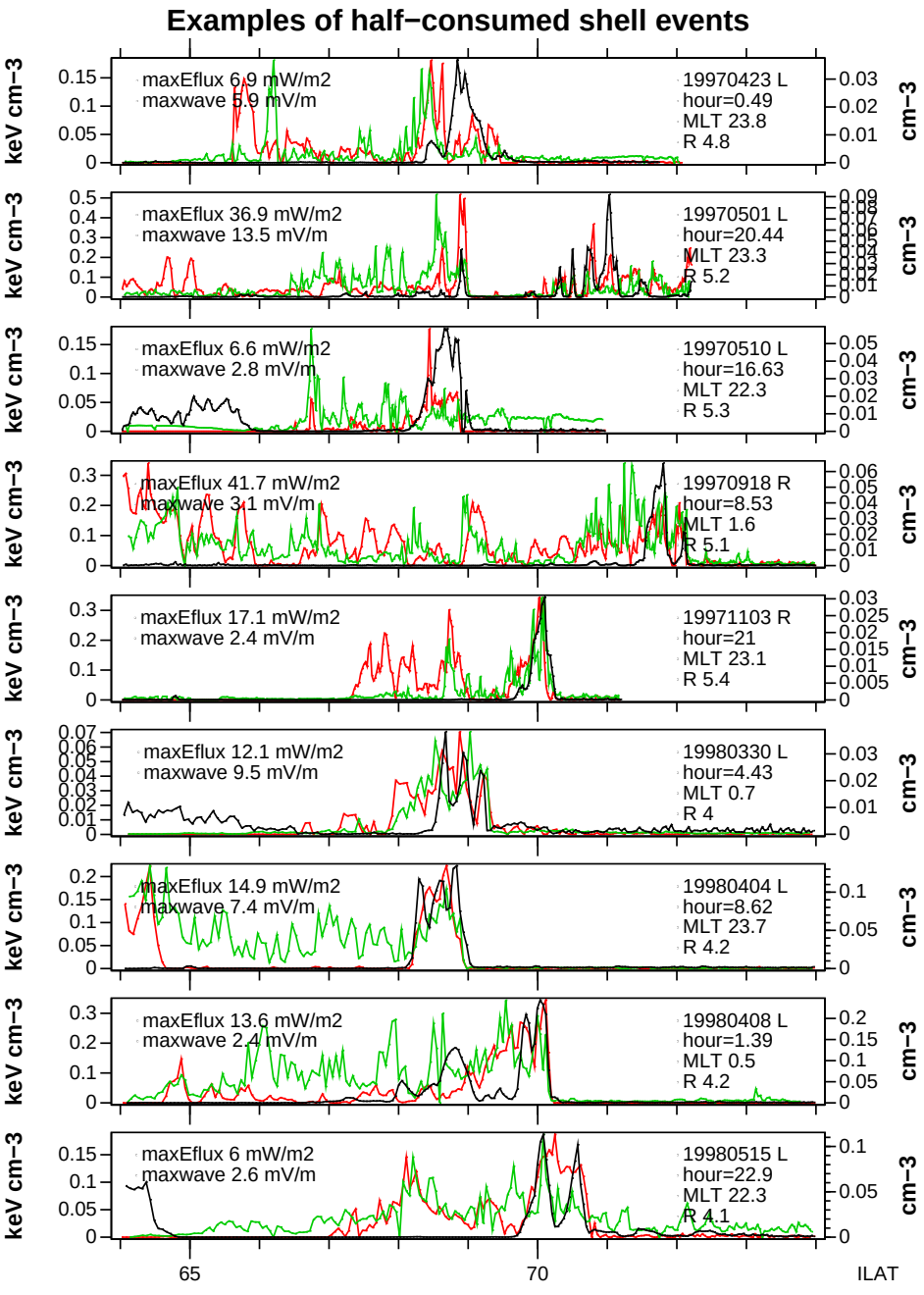

Fig. 14. Examples of half-consumed shell events. Each panel is one event. Black line is free energy from TIMAS (scale on the left) and red line is magnitude of electron anisotropy from HYDRA (scale on the right). Green line is unnormalised perpendicular wave power from EFI (12-s averaged); its attained maximum is written on the left ("maxwave"). Maximum downward ion energy flux from TIMAS during time when free energy exceeds 0.02 keV cm^{-3} is also given; the value is given at the ionospheric level by multiplying the measured value by flux tube scaling factor. Event date and average UT-hour, MLT and radial distance are also given. The letter L(R) after the date indicates that the satellite is moving to the left (right), i.e. towards decreasing (increasing) ILAT.

From Fig. 14 one sees that usually the largest free energy densities occur in the PSBL, i.e. near the polar cap boundary. In some of the plots one also sees CPS shells at low ILAT. In many cases the electron anisotropies and waves correlate in a broad sense with the free energy density, at least in the sense that cases with high free energy density near the polar cap boundary (PSBL) are almost always associated with strong waves and anisotropies close to that boundary as well. Further away from the polar cap boundary (i.e. in the BPS) one often sees anisotropies and waves without free energy density nearby, but the amplitude of the waves and anisotropies is typically less than in the PSBL.

8 Summary and discussion

The ion shells in the ILAT range 65–75 can be separated into CPS and PSBL/BPS ion shells. The CPS ion shells differ from the PSBL shells in many respects: they are on the average more energetic, they have wide loss-cones, they are not related to electron anisotropy or wave activity and they typically have a long duration in Polar data (wide ILAT coverage). Many of them are probably related to ion spectral gaps (Buzulukova et al., 2002). In this paper we have concentrated on the PSBL ion shells (they sometimes occur in the BPS also) since they may play an important role in the energy exchange in the auroral zone. We now summarise our main observational findings regarding auroral zone ion shells.

1. Ion shells consist almost exclusively of hydrogen only.
2. When the free energy density is significant ($>0.1\,\mathrm{keV/cm^3}$), the shell is almost always close to the polar cap boundary, i.e. they are in the PSBL (Fig. 1 panel (c)). Lower energy shells (panel (b)) may appear in the BPS, too, but also they are most common in the PSBL.
3. If a threshold of $20\,\mathrm{eV\,cm^{-3}}$ is chosen for the free energy density, PSBL ion shells have an occurrence frequency of 5% (spread over a few degrees because the polar cap boundary location varies from case to case), Fig. 1 panel (b).
4. Plateaued distributions, which we interpret as partly or completely consumed remnants of shell distributions, are common in the BPS.
5. Partly consumed ion shells are associated with wave activity and middle-energy (100–1000 eV) electron anisotropy (Fig. 14).
6. The total ion downward energy flux associated with ion shell distributions is $\sim 15\,\mathrm{mW\,m^{-2}}$ in many events, but can be as large as $42\,\mathrm{mW\,m^{-2}}$ (Fig. 14 panel (4)).
7. Although we used the frequency range 1–10 Hz to measure wave activity in most cases, higher frequencies (10–500 Hz) are also usually excited at the same time (Fig. 11 panel (a)).
8. A clear energy/latitude dispersion is seen, where higher ILAT corresponds to higher shell energy, until some cutoff at which the shell disappears (so-called velocity-dependent ion signature (VDIS) events).
9. PSBL/BPS ion shells are always associated with an upgoing ion beam, which typically has much smaller energy than the shell. Typically, the ion beam contains both H+ and O+ in significant amounts.
10. A clearly identifiable CPS/BPS boundary in the MLT-ILAT plane can be seen in the statistics, which moves with K_p in a way which is consistent with a statistical oval model (Fig. 1).
11. In the PSBL/BPS, free and consumed energy densities mainly concentrate in the midnight MLT sector for low K_p, but they are more spread in MLT for high K_p (Figs. 1 and 7).
12. Neither the free energy density nor the consumed energy density shows marked altitude dependence below R=6 R_E (Figs. 1 and 7).
13. While the average free energy density u (Fig. 1) is minimal in the BPS, the so-called consumed energy density u_{cons} (Fig. 7) is larger there.
14. The consumed free energy density u_{cons} is enhanced at subauroral latitudes in the postnoon sector, which probably follows from ion motion (Fig. 8).

The observational results summarised above concerning auroral zone ion shells give rise to some important physical questions. We will discuss these questions below.

The PSBL ion shells usually have an energy-latitude dispersion and are probably closely related to VDIS events (Elphic and Gary, 1990; Baumjohann et al., 1990; Zelenyi et al., 1990). The VDIS ions are thought to originate in the magnetotail as earthward moving beamlets (Speiser, 1965; Ashour-Abdalla et al., 1992; Bosqued et al., 1993b; Ashour-Abdalla et al., 1993, 1995). These test particle simulations by Ashour-Abdalla and coworkers follow the motion of ions in two-dimensional Tsyganenko model field and constant GSM Y-directed electric field. They show that ions are injected earthward in the non-adiabatic region of the tail, where the κ parameter ($\kappa=\sqrt{R_{\mathrm{curv}}/r_{iL}}$, R_{curv} is the curvature radius of the magnetic field and r_{iL} is the ion Larmor radius in the equatorial plane) is smaller than unity. The ions gain energy from electrostatic acceleration since their motion is temporarily not governed by the magnetic field. The simulations show structure (beamlet) formation at two levels. First, there are critical values of κ given by $\kappa_n^{\mathrm{crit}}\approx 0.8/(n+1/2)$, n=1, 2, 3, ... where the ions most easily spend a long time in the current sheet gaining energy from the electric field. Second, each beamlet bounces multiple times (labelled by k) across the equatorial plane while being convected earthward by the $E\times B$ drift (Ashour-Abdalla et al., 1995).

A monoenergetic earthward moving ion beamlet having some angular spread is turned by the mirror force into a shell distribution at sufficiently low altitude (most probably, the altitude is sufficiently low in this case in the present paper). If the beamlet is not monoenergetic, the $E\times B$ drift combines with the time-of-flight effect to produce, in addition, an energy-latitude dispersion, i.e. a VDIS. A somewhat similar dispersion is also produced by the fact that beamlets with different integer index n (see above) have different energies; however, if a smooth VDIS is seen, it most probably corresponds to only one n value and thus is a time-of-flight effect. Beamlets with different n and k indices mix, the mixing loci forming a spatial mosaic structure (Ashour-Abdalla

et al., 1995). When mixing occurs, a clear shell distribution is not seen. In TIMAS data there are cases where two or more shells at different energies are seen at the same time.

The CPS shells are most probably not formed by these process. One possibility for their formation is the energy dependence of azimuthal drift velocity, i.e. a competition between the energy-independent $E \times B$ drift and the energy-dependent gradient and curvature drifts. This mechanism might also contribute to the formation of PSBL and BPS shells.

We found many cases where a shell is partly consumed (1/4-consumed, half-consumed, 3/4-consumed, etc.). At least one way to interpret a half-consumed shell, for example, is to assume that the observation point is at the upper boundary of a region where a shell-consuming wave-particle interaction takes place. Likewise, a 1/4-consumed shell corresponds to a situation where the consumption process resides at some distance below the observation point. In more complicated cases, one may need to also assume a temporal turning on or off of the consumption process. If the energy is fixed, the pitch angle of a particle tells how long ago the particle passed through the equatorial plane: this time is shortest for zero pitch angle (downgoing) particles and longest for exactly upgoing ones (180° pitch angle). The upgoing particles have mirrored below the observation point which has taken extra time. If the consumption process worked in the past but stopped some time ago, particles launched after stopping are not affected by it, and in the distribution function they are particles whose pitch angle is smaller than some limit.

What is the role of auroral zone shell distributions in powering auroral phenomena? The largest downward ion energy flux that occurred in a shell distribution was $42\,\mathrm{mW\,m^{-2}}$ and values above $10\,\mathrm{mW\,m^{-2}}$ are not rare. This is not as large as the $100\,\mathrm{mW\,m^{-2}}$ or so, which is required to power the most intense substorm aurorae (and which is available from Alfvénic Poynting flux in at least some of those cases, Wygant et al., 2000), but it could be enough to power stable auroral arcs. If the ion shell distributions are part of the energy transfer chain causing auroral arcs, the whole chain would be something like the following (see also Olsson and Janhunen, 2004):

1. Ions are energised in the magnetotail in the non-adiabatic low-B_z region and injected towards the Earth (Ashour-Abdalla et al., 1995). If the ions are injected as field-aligned beams, the distribution function turns into a shell distribution at lower altitudes because of the mirror force or because of the time-of-flight effect, or both.

2. At some altitude, the combination of magnetic field and plasma conditions are such that the shell distribution becomes unstable to waves which consume its free energy. Specifically, it has been shown that ion Bernstein waves are created by a shell distribution (Janhunen et al., 2003a). In any case, the altitude where this happens is still unclear. The altitude must be low enough that the shell distribution has already formed by the mirror force from the earthward moving beamlets.

3. The waves generated by the shell distribution energise middle-energy electrons (Janhunen et al., 2003a, 2004a) in the parallel direction, producing a middle-energy $T_\parallel > T_\perp$ electron distribution superposed with isotropic hot (and possibly cold) electron backgrounds.

4. A downward parallel electric field is set up because otherwise, the $T_\parallel > T_\perp$ type electron distribution would create a negative charge cloud at low altitudes which is not possible since the plasma must be quasi-neutral.

5. Since the system in long time-scales must behave electrostatically, the parallel electric field must be part of a potential structure. Because the ionosphere is approximately in constant potential (the ionospheric perpendicular fields are much smaller than the strong perpendicular fields that exist in the acceleration region), the only way to close the potential contours is with a closed negative potential structure.

6. The lower part of the potential structure accelerates electrons downward and produces peaked inverted-V electron spectra at low altitude which are also the main contributors to the optical emissions. Electrons can enter the closed negative structure with the help of the above-mentioned Bernstein waves.

Many parts of the process chain described above have been found to be in agreement with data or reproduced by simulations. For a recent review, see Olsson and Janhunen (2004).

To model shell distribution formation, one should apply similar test particle simulations that has been carried out by Ashour-Abdalla et al. (1995), but for a larger set of particles, so that enough statistics of beamlet ions can be gathered also below $6\,R_E$. The distributions of these beamlets could then be studied and compared with the observed ion shells discussed in this paper.

Acknowledgements. We are grateful to C. A. Kletzing and J. D. Scudder for providing HYDRA data, H. Laakso and F. S. Mozer for EFI data, J. S. Pickett, D. A. Gurnett for PWI data and C. T. Russell for MFE data. The work of PJ was supported by the Academy of Finland and that of AO by the Swedish Research Council.

The Editor in Chief thanks two referees for their help in evaluating this paper.

References

Ashour-Abdalla, M., Zelenyi, L. M., Bosqued, J.-M., Peroomian, V., Wang, Z., Schriver, D., and Richard, R. L.: The formation of the wall region: consequences in the near Earth magnetotail, Geophys. Res. Lett., 19, 1739–1742, 1992.

Ashour-Abdalla, M., Berchem, J. P., Büchner, J., and Zelenyi, L. M.: Shaping of the magnetotail from the mantle: global and local structuring, J. Geophys. Res., 98, 5651–5676, 1993.

Ashour-Abdalla, M., Zelenyi, L. M., Peroomian, V., Richard, R. L., and Bosqued, J. M.: The mosaic structure of plasma bulk flows in the Earth's magnetotail, J. Geophys. Res., 100, 19 191–19 209, 1995.

Baumjohann, W., Paschmann, G., and Lühr, H.: Characteristics of high-speed ion flows in the plasma sheet, J. Geophys. Res., 95, 3801–3809, 1990.

Bingham, R., Kellett, B. J., Cairns, R. A., Dendy, R. O., and Shukla, P. K.: Wave generation by ion horseshoe distributions on auroral field lines, Geophys. Res. Lett., 26, 2713–2716, 1999.

Bosqued, J. M., Ashour-Abdalla, M., El Alaoui, M., Zelenyi, L. M., and Berthelier, A.: AUREOL-3 observations of new boundaries in the auroral ion precipitation, Geophys. Res. Lett., 20, 1203–1206, 1993.

Bosqued, J. M., Ashour-Abdalla, M., El Alaoui, M., Peroomian, V., Zelenyi, L. M., and Escoubet, C. P.: Dispersed ion structures at the poleward edge of the auroral oval: Low-altitude observations and numerical modeling, J. Geophys. Res., 98, 19 181–19 204, 1993a,b.

Buzulukova, N. Y., Galperin, Y. I., Kovrazhkin, R. A., Glazunov, A. L., Vladimirova, G. A., Stenuit, H., Sauvaud, J. A., and Delcourt, D. C.: Two types of ion spectral gaps in the quiet inner magnetosphere: Interball-2 observations and modelin, Ann. Geophys., 20, 349–364, 2002.

Ejiri, M.: Trajectory traces of charged particles in the magnetosphere, J. Geophys. Res., 83, 4798–4810, 1978.

Eliasson, L., André, M., Eriksson, A., Nordqvist, P., Norberg, O., Lundin, R., Holback, B., Koskinen, H., Borg, H., and Boehm, M.: Freja observations of heating and precipitation of positive ions, Geophys. Res. Lett., 21, 1911–1914, 1994.

Elphic, R. C. and Gary, S. P.: ISEE observations of low frequency waves and ion distribution function evolution in the plasma sheet boundary layer, Geophys. Res. Lett., 17, 2023–2026, 1990.

Engebretson, M. J., Peterson, W. K., Posch, J. L., Klatt, M. R., Anderson, B. J., Russell, C. T., Singer, H. J., Arnoldy, R. L., and Fukunishi, H.: Observations of two types of Pc-1–2 pulsations in the outer dayside magnetosphere, J. Geophys. Res., 107, 1451–1471, 2002.

Gurnett, D. A., Persoon, A. M., Randall, R. F., Odem, D. L., Remington, S. L., Averkamp, T. F., Debower, M. M., Hospodarsky, G. B., Huff, R. L., Kirchner, D. L., Mitchell, M. A., Pham, B. T., Phillips, J. R., Schintler, W. J., Sheyko, P., and Tomash, D. R.: The polar plasma wave instrument, edited by Russell, C. T., Kluwer Acad., Space Sci. Rev., 71, 597–622, 1995.

Harvey, P., Mozer, F. S., Pankow, D., Wygant, J., Maynard, N. C., Singer, H., Sullivan, W., Anderson, P. B., Pfaff, R., Aggson, T., Pedersen, A., Falthammar, C. G., and Tanskanen, P.: The electric field instrument on the polar satellite, Space Sci. Rev., 71, 583–596, 1995.

Holzworth, R. H. and Meng, C.-I.: Mathematical representation of the auroral oval, Geophys. Res. Lett., 2, 377–380, 1975.

Janhunen, P., Olsson, A., Vaivads, A., and Peterson, W. K.: Generation of Bernstein waves by ion shell distributions in the auroral region, Ann. Geophys., 21, 1–11, 2003a.

Janhunen, P., Olsson, A., and Peterson, W. K.: The occurrence frequency of upward ion beams in the auroral zone as a function of altitude using Polar/TIMAS and DE-1/EICS data, Ann. Geophys., 21, 2059–2072, 2003b.

Janhunen, P., Olsson, A., Laakso, H., and Vaivads, A.: Middle-energy electron anisotropies in the auroral region, Ann. Geophys., 22, 1–13, 2004a.

Karimabadi, H., Krauss-Varban, D., Omidi, N., Fuselier, S. A., and Neugebauer, M.: Low-frequency instabilities and the resulting velocity distributions of pickup ions at comet Halley, J. Geophys. Res., 99, 21 541–21 556, 1994.

Klumpar, D. M., Peterson, W. K., and Shelley, E. G.: Direct evidence for two-stage (bimodal) acceleration of ionospheric ions, J. Geophys. Res., 89, 10 779–10 787., 1984.

Kucharek, H. and Scholer, M.: Injection and acceleration of interstellar pickup ions at the heliospheric termination shock, J. Geophys. Res., 100, 1745–1754, 1995.

Malingre, M., Dubouloz, N., Berthelier, J. J., Galperin, Y., Chugunin, D., Perraut, S., Sauvaud, J. A., Delcourt, D., and Stepanov, V.: Low-energy upflowing ion events at the poleward boundary of the nightside auroral oval: high-altitude Interball-Auroral Probe observations, J. Geophys. Res., 105, 18 693–18 707, 2000.

McIlwain, C.: Plasma convection in the vicinity of the geosynchronous orbit, Earth's Magnetospheric Processes, edited by McCormac, B., 262, D. Reiderl Pub. Comp., 1972.

Olsson, A. and Janhunen, P.: Some recent developments in understanding auroral electron acceleration processes, IEEE Trans. Plasma Sci., in press, 2004.

Onsager, T. G. and Mukai, T.: Low altitude signature of the plasma sheet boundary layer: Observations and model, Geophys. Res. Lett., 22, 855–858, 1995.

Press, W. H., Teukolsky, S. A., Vetterling, W. T., and Flannery, B. P.: Numerical Recipes in C, The art of scientific computing, 2nd ed., Cambridge, 1992.

Russell, C. T., Snare, R. C., Means, J. D., Pierce, D., Dearborn, D., Larson, M., Barr, G., and Le, G.: The GGS/Polar Magnetic Fields Investigation, Space Sci. Rev., 71, 563–582, 1995.

Scudder, J. D., Hunsacker, F., Miller, G., Lobell, J., Zawistowski, T., Ogilivie, K., Keller, J., Chornay, D., Herrero, F., Fitzenreiter, R., Fairfield, D., Needell, J., Bodet, D., Googins, J., Kletzing, C., Torbert, R., Vandiver, J., Bentley, R., Fillius, W., McIlwain, C., Whipple, E., and Korth, A.: Hydra – A 3-dimensional electron and ion hot plasma instrument for the Polar spacecraft of the GGS mission, Space Sci. Rev., 71, 459–495, 1995.

Shelley, E. G., Ghielmetti, A. G., Balsiger, H., Black, R. K., Bowles, J. A., Bowman, R. P., Bratschi, O., Burch, J. L. , Carlson, C. W., Coker, A. J., Drake, J. F., Fischer, J., Geiss, J., Johnstone, A., Kloza, D. L., Lennartsson, O. W., Magoncelli, A. L., Paschmann, G., Peterson, W. K., Rosenbauer, H., Sanders, T. C., Steinacher, M., Walton, D. M., Whalen, B. A., and Young, D. T.: The Toroidal Imaging Mass-Angle Spectrograph (TIMAS) for the Polar Mission, Space Sci. Rev., 71, 1–4, 1995.

Shirai, H., Maezawa, K., Fujimoto, M., Mukai, T., Saito, Y., and Kaya, N.: Monoenergetic ion drop-off in the inner magnetosphere, J. Geophys. Res., 102, 19 873–19 881, 1997.

Speiser, T. W.: Particle trajectories in model current sheets, J. Geophys. Res., 70, 4219–4226, 1965.

Winningham, D., Yasuhara, F., Akasofu, S.-I., and Heikkila, W. J.: The latitudinal morphology of 10-eV to 10-keV electron fluxes during magnetically quiet and disturbed times in the 21:00–03:00 MLT sector, J. Geophys. Res., 80, 3148–3171, 1975.

Wygant, J. R., Keiling, A., Cattell, C. A., Johnson, M., Lysak, R. L., Temerin, M., Mozer, F. S., Kletzing, C. A., Scudder, J. D., Peterson, W., Russell, C. T., Parks, G., Brittnacher, M., Germany, G., and Spann, J.: Polar spacecraft based comparisons of intense electric fields and Poynting flux near and within the plasma sheet-tail lobe boundary to UVI images: an energy source for the aurora, J. Geophys. Res., 105, 18 675–18 692, 2000.

Zelenyi, L. M., Kovrazkhin, R. A., and Bosqued, J. M.: Velocity-dispersed ion beams in the nightside auroral zone: AUREOL 3 observations, J. Geophys. Res., 95, 12 119–12 139, 1990.